

Quantum imaging at 10 volumetric images per second

GIANLORENZO MASSARO,^{1,2,4} PAUL MOS,^{3,4} SERGII VASIUKOV,^{2,4}
 FRANCESCO DI LENA,^{2,5} FRANCESCO SCATTARELLA,^{1,2,5}
 FRANCESCO V. PEPE,^{1,2,*} ARIN ULKU,³ DAVIDE GIANNELLA,^{1,2}
 EDOARDO CHARBON,³ CLAUDIO BRUSCHINI,^{3,6} AND
 MILENA D'ANGELO^{1,2,6}

¹*Dipartimento Interateneo di Fisica, Università degli Studi di Bari, Bari, I-70126, Italy*

²*Istituto Nazionale di Fisica Nucleare, Sezione di Bari, Bari, I-70125, Italy*

³*Ecole polytechnique fédérale de Lausanne (EPFL), Neuchâtel, 2002, Switzerland*

⁴*The authors contributed equally to this work*

⁵*The authors contributed equally to this work*

⁶*The authors contributed equally to this work*

*francesco.pepe@ba.infn.it

Abstract: The correlation properties of light provide an outstanding tool to overcome the limitations of traditional imaging techniques. A relevant case is represented by correlation plenoptic imaging (CPI), a quantum imaging protocol employing spatio-temporal correlations to address the main limitations of conventional light-field imaging, namely, the poor spatial resolution and the reduced change of perspective for 3D imaging. However, the application potential of high-resolution quantum imaging is limited, in practice, by the need to collect a large number of frames to retrieve correlations. This creates a gap, unacceptable for many relevant tasks, between the time performance of quantum imaging and that of traditional imaging methods. In this article, we address this issue by exploiting the photon number correlations intrinsic in chaotic light, in combination with a cutting-edge ultrafast sensor made of a large array of single-photon avalanche diodes (SPADs). A novel single-lens CPI scheme is employed to demonstrate quantum imaging at an acquisition speed of 10 volumetric images per second. Our results place quantum imaging at a competitive edge and prove its potential in practical applications.

1. Introduction

The idea of using quantum correlations to overcome classical limits in the acquisition of information, as applied to imaging, metrology, and sensing, was one of the earlier signs of the so-called second quantum revolution. Though the target has gradually extended towards quantum communication, computation, and simulation, imaging and related tasks remain a pillar of the ongoing breakthrough. Novel quantum-inspired imaging modalities have been developed throughout the years to address enhancement in resolution (either transverse or volumetric), spectral range, contrast, signal-to-noise ratio (SNR) (see Refs. [1–3] for recent reviews). Moreover, the quantum properties of light open the possibility to perform entirely new tasks, such as imaging with undetected photons [4], imaging of objects hidden to the main sensor [5, 6], using different wavelengths for sample illumination and light detection [7–9], identifying objects surrounded by turbulence [10–12], beating the shot-noise limit [13–16]. The peculiar correlations of photons in time, position, momentum and energy, that characterize specific quantum states, are crucial to achieve any improvement [17]. Though the initial schemes relied on the properties of entangled photon pairs generated by parametric down-conversion [18, 19], it was soon discovered that specific tasks could be achieved even by using correlated beams of chaotic (*e.g.*, pseudothermal) light [20–24], typically at the expense of SNR [25, 26], but with the advantage of a simpler and more feasible light production scheme, also avoiding the low production rate of entangled

photons.

The variety of advantages entailed by the spatio-temporal correlation properties of light clashes with the most relevant challenge of quantum imaging: reducing the acquisition time for making it effectively competitive with the corresponding state-of-the-art traditional techniques. Such a challenge is intrinsic to this approach, since correlation functions require sampling a high enough number of statistical realizations in order to be reconstructed. The use of high-resolution cameras in correlation imaging setups [2, 3, 20, 23, 27–29] has enabled to overcome the extremely time-consuming spatial sampling, which was performed in the pioneering quantum imaging experiments [18], at the expense of detector response times. There are two time scales that one must consider when dealing with the speed of quantum imaging with a camera [3]. First, if N_t camera frames are required, the *total acquisition time* is equal to $T_{\text{image}} = N_t/R$, with R the frame rate, and its inverse, T_{image}^{-1} , is the rate at which correlation images can be acquired. The acquisition rate can be kept small by i) employing high-speed sensors, and ii) optimizing the trade-off between number of frames and SNR, with the latter expected to depend on $\sqrt{N_t}$ [25, 30–33]. The other crucial time scale to be considered is the *gating time*, namely, the effective sensitivity window in which a single frame is acquired: if this is larger than the source coherence time, intensity fluctuations in each frame are partially erased [34], making it more difficult to reconstruct their correlations, and thus increasing N_t . To fulfill such temporal requirements, recent quantum imaging experiments have started employing a novel class of detectors, made of an arrays of single-photon avalanche photodiodes (SPADs) [35–38]. SPAD arrays ensure at once fast acquisition rates, short gating times, and low noise, which is essential for high-quality sampling of the light statistics. SPAD arrays with different resolutions have already been successfully applied to quantum imaging, providing significant advantages in gating time and low frame noise [39, 40]; however, the low production rate of entangled photons led to acquisition times much larger than one second. On the other hand, low-resolution (32×32) SPAD arrays have been used in computational ghost imaging experiments to obtain 1 000 two-dimensional images per second. It is also worth mentioning a recent experiment achieving sub-second acquisition times in chaotic-light ghost imaging with an intensified CCD triggered by a single SPAD [41], as well as the recent achievement of a few-second acquisition time with a high resolution (256×256) time-tagging camera, in an experiment oriented to correlation detection rather than to imaging [42].

In this work, we shall demonstrate quantum images at a rate of 10 acquisitions per second. The key for achieving such a performance is the use of SwissSPAD2 [35–37, 43], a SPAD array operated at a 512×256 -pixel resolution, and capable of acquiring up to 10^5 frames per second. This is combined with the use of chaotic light illumination, which enables to avoid the low speed related with the low production rates of parametric down-conversion. Specifically, we shall show how correlations can be exploited to obtain *volumetric* images at the aforementioned rate, relying on the principles of correlation plenoptic imaging (CPI) [44–48]. This technique enables to acquire light-field images, which contain information about both the spatial distribution of light and its propagation direction. Such a richness of information can be used, during data processing, to reconstruct light paths and obtain a three-dimensional snapshot of the scene of interest. In particular, one can *refocus* the images of specific transverse planes of the scene, which were out of focus at the moment of the capture. In traditional light-field imaging devices [49–52], based on the insertion of an array of micro-lenses before the sensor, directional resolution can be gained only at the expense of spatial resolution [53]. Nonetheless, aided by additional post-processing algorithms [54–56], they find applications in the most diverse fields, such as photography [57] and microscopy [58]. Light-field cameras based on intensity measurement can currently operate at the essentially same rates of a standard camera, which evidently outperforms any quantum imaging technique (volumetric or not) at similar resolutions. However, many interesting applications of light-field imaging in science, including the neuronal activity detection accomplished in

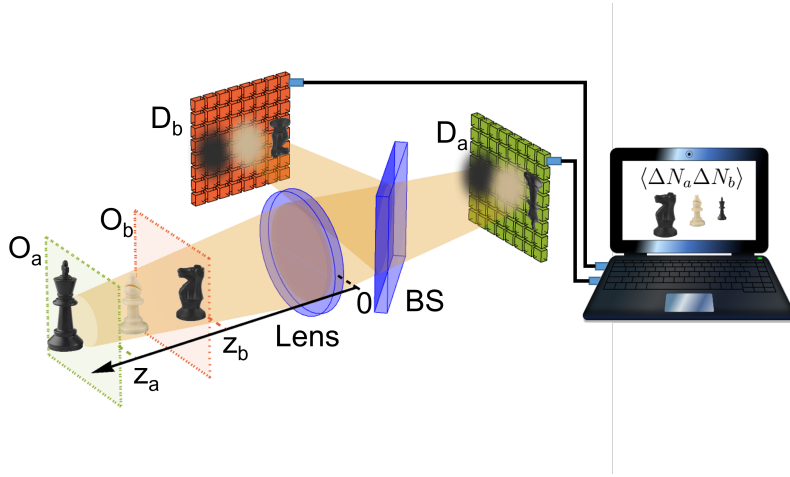


Fig. 1. Working principle of the developed CPI protocol. O_a and O_b are the two conjugate planes of the high-resolution sensors D_a and D_b ; they are placed at the generic distances z_a and z_b from the lens, respectively. BS is a beam splitter sending light from the lens toward the two sensors. Pixel-by-pixel correlations between photon number fluctuations are evaluated by software and employed to reconstruct the volumetric image of the scene. See Sec. 4 for the detailed experimental setup.

Refs. [59, 60], are performed at image rates ranging between 10 and 100 Hz [60, 61]. The results presented in this paper demonstrate the competitiveness of quantum imaging in these tasks: CPI brings a net advantage with respect to state-of-the-art cameras, combining similar time performances with an improved volumetric resolution at analogous numerical aperture [47, 62]. To the best of our knowledge, the presented CPI setup is indeed the first case of a feasible light-field device employing a single lens.

The article is organized as follows. In Sec. 2, we summarize the working principle of the novel CPI device and show the possibility to obtain lightfield images with a 0.1 s acquisition time. In Sec. 3, we highlight the relevance of our results along with their implications for practical applications, and discuss both the current limitations of our experiment and the foreseen future developments. Sec. 4, we present details about the experimental setup. The Supplement 1 document further details on the measured correlation functions and the refocusing process, as well as complementary results on the interdependence between the number of collected frames (hence, the image acquisition time) and the SNR.

2. Results

The working principle of the CPI camera is reported in Fig. 1 [47]. Two planes O_a and O_b , chosen arbitrarily within the three-dimensional scene of interest, are focused on two high-resolution sensors, D_a and D_b . Unlike a conventional light-field camera, involving both the usual camera lens and a micro-lens array, our CPI device is realized with a single lens, collecting light from both chosen planes, and focusing them on the two sensors. Light from the scene is chaotic; hence, by computing the equal-time pixel-by-pixel correlation between the number of photons (N_a and N_b) detected by the sensors D_a and D_b , we obtain the correlation function:

$$\Gamma(\boldsymbol{\rho}_a, \boldsymbol{\rho}_b) = \langle N_a(\boldsymbol{\rho}_a) N_b(\boldsymbol{\rho}_b) \rangle - \langle N_a(\boldsymbol{\rho}_a) \rangle \langle N_b(\boldsymbol{\rho}_b) \rangle, \quad (1)$$

where $\langle \dots \rangle$ indicates the averaging process, while $\boldsymbol{\rho}_a$ and $\boldsymbol{\rho}_b$ are the coordinates identifying pixel positions on the sensors. The correlation function in Eq. (1) contains plenoptic information,

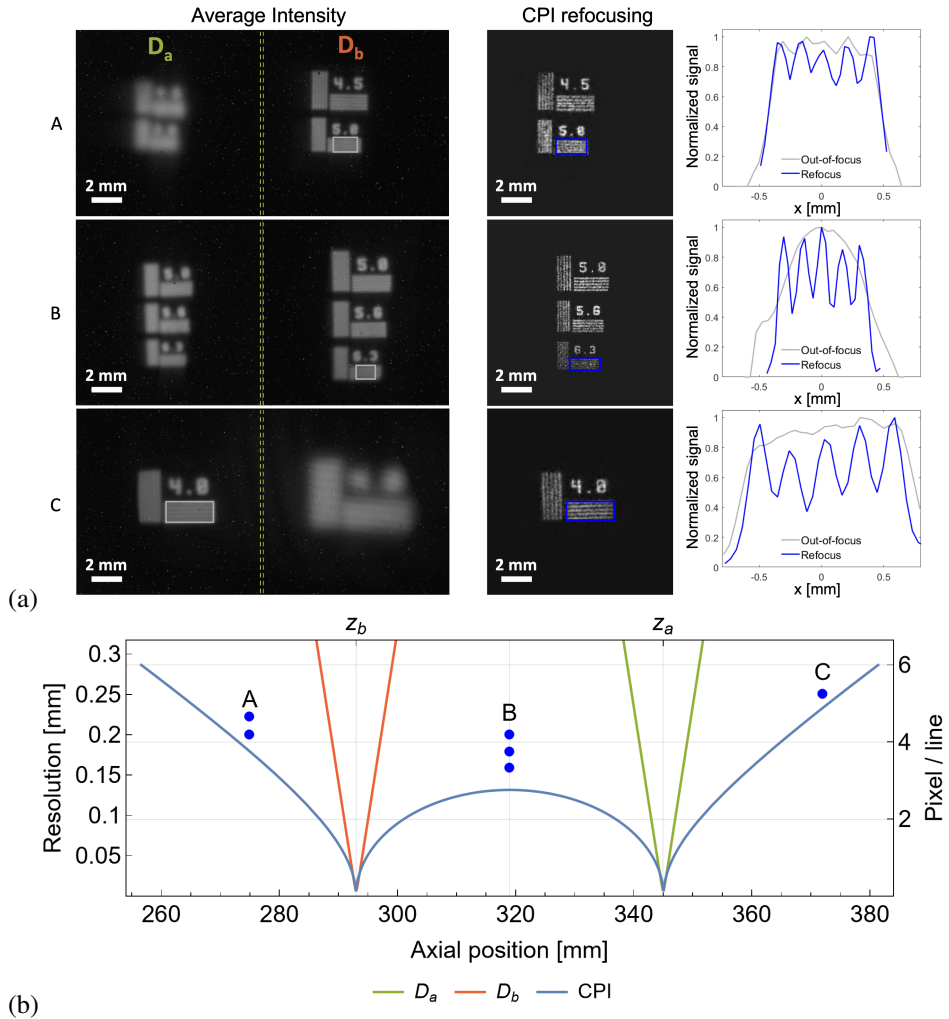


Fig. 2. (a) Comparison between the images directly retrieved by the sensors, through their average intensity (left panels), and the images refocused by means of CPI (central panel); the plots in the right panel are obtained by integrating the highlighted rectangles in the corresponding average intensities (gray) and refocused images (blue) along the slit direction. All the reported data have been obtained by acquiring $N_t = 9.8 \times 10^3$ frames, at full resolution, at $\sim 9.8 \times 10^4$ frames per second, resulting in an overall acquisition speed of 10 volumetric images per second. (b) Comparison of the resolution achieved by conventional imaging (orange for D_b , green for D_a) and CPI (blue) as a function of the axial distance from the lens. A ($z = 275$ mm), B ($z = 319$ mm) and C ($z = 373$ mm) indicate the three different masks shown in panels (a); the plot shows their axial position and the distances between neighboring slits within the masks.

and thus enables reconstructing features of a 3D object that can be placed both between and beyond the two planes O_a and O_b imaged on the detectors [46, 63]. As explained in detail in Supplement 1, $\Gamma(\rho_a, \rho_b)$ encodes a collection of multi-perspective volumetric images; proper processing of these volumetric images provides the *refocused image* of a specific transverse plane in the scene.

Experimental results are reported in Fig. 2: Both sensors acquire blurred images of three different planar test targets (A, B, and C); the plenoptic information contained in the measured correlation function enables reconstructing the object details, in all three cases. In the panel on the left, we report the out-of-focus images of the test target, which is placed either within (case B) or outside (cases A and C) the volume defined by the two conjugate planes of the detectors; the effective refocusing enabled by CPI is shown in the center panels. The recovery in visibility deriving from refocusing is demonstrated in the right panels: here, we compare the linear images related with both average intensity and CPI, which are obtained by integration along the slit direction. CPI also enables over $10\times$ depth of field (DOF) enhancement at a resolution of $250\ \mu\text{m}$, and $12\times$ at $160\ \mu\text{m}$, with respect to a conventional imaging system with the same numerical aperture (NA). This can be seen by considering the curves reported in panel (b) of Fig. 2, together with the axial position and the distance between neighboring slits on the three test targets (A, B, and C) reported in panel (a). The plot shows the expected resolution limit of the refocused images (blue line), with varying axial position z , compared with the analogous limits associated with the conventional images focused on D_a (green line) and D_b (orange line). In particular, the blue line indicates the object detail size (i.e., the resolution) that can be refocused by our CPI device with 10% visibility, as a function of the longitudinal distance (z) of the object from the lens. The green and red lines represent the natural DOF (as determined by the circle of confusion) of the images separately observed on the two sensors D_a and D_b , at the given resolution.

The images reported in Fig. 2 have been obtained at an overall acquisition speed of 10 volumetric images per second. This is an unprecedented result in the field of quantum imaging, and indicates the feasibility of quantum imaging at video rate. The noise analysis reported in Supplement 1 shows the robustness of the developed technique: when the acquisition speed is reduced to 1 image per second by increasing the number of acquired frames by 1 order of magnitude, the SNR increases by nearly 35%, and reaches its maximum value. A comparison between the CPI images acquired at the speed of 1 and 10 volumetric images per second is reported in Fig. S3 of Supplement 1.

3. Discussion

We have presented a quantum imaging system capable of collecting 10 plenoptic images per second. Since plenoptic images are a collection of multi-perspective volumetric images, they enable changing, in post-processing, the focusing plane within the entire axial range enclosed by the blue curve in Fig. 2b). This result entails a large reduction of the gap in time-performance between CPI and conventional light-field imaging, that is generally performed at a speed between 10 and 100 Hz, in scientific applications [60, 61], but with a significant loss of resolution due to microlens array and intensity measurement.

The key element to achieve such a critical improvement in the acquisition time is the integration of the SwissSPAD2 sensor in a chaotic-light based correlator plenoptic imaging setup. This SPAD array enables to collect, with single-photon sensitivity, all the frames that contribute to the plenoptic correlation image, at a rate of almost 100.000 frames per second. Such a fast rate is combined with both a resolution comparable to that of ordinary detectors and low noise (see Refs. [36, 37, 43] for a detailed description of the sensor). The low noise of the detector is a key aspect for keeping as low as possible the number of frames N_t required for reconstructing light statistics and correlations. Our SwissSPAD2 sensor has an on-board DDR3 memory bank (2 GB) that can be filled with a maximum of 131 072 measured binary frames. By saving the acquired

data on the internal memory instead of streaming to an external disk, we were able to exploit the maximum speed of 97.7 kHz at full resolution. However, the limited capacity of the memory has bound us to single-image acquisitions instead of videos. In the future, we shall employ a new generation of SwissSPAD2 capable of streaming data from a 512×512 sensor to a workstation at full speed.

The new generation of SwissSPAD2 also provides a relevant improvement in the gating time, which can be reduced down to about 10 ns. This represents an extremely important parameter in correlation imaging based on chaotic light, since reconstruction of light statistics is optimal when the detector exposure time matches the coherence time of light [34]. The possibility to match coherence times as small as hundreds of ps would open the way to CPI with broadband sources, thus leading the way toward passive quantum imaging devices.

It is reasonable to expect the achieved acquisition speed to be further increased through computational techniques enabling to use less frames to achieve a comparable SNR; examples are compressive sensing [64, 65], quantum tomography [66], and machine learning [67]. All these techniques are currently being developed in the framework of CPI, and we plan to integrate them with our refocusing algorithm [43]. To further increase the SNR while reducing the acquired number of frames, we are also working toward employing, within the data analysis, the statistical properties of the correlation function, in a similar fashion as in [68]. It is interesting to emphasize, however, that all data presented in this work have not been treated with any denoising algorithm, or post-processing method, other than the refocusing algorithm described in Supplement 1.

The novelty of the implemented CPI setup also stands in the fact that two arbitrary planes are focused on the two sensors [47], as opposed to conventional approaches involving imaging of the main lens for retrieving directional information. This approach enables: (i) parallel acquisition of two diffraction limited images within the three-dimensional scene of interest, (ii) *single-lens light-field imaging*, which is quite significant considering the disadvantages and physical limitations connected with the use of micro-lenses (i.e., resolution loss and reduced 3D imaging capability), (iii) a DOF enhancement by over 1 order of magnitude, without sacrificing diffraction-limited resolution.

4. Materials and Methods

The optical system is aimed at maximizing speed of acquisition and performance in terms of resolution versus DOF trade-off, while guaranteeing flexibility in the focusing capability. The design of the employed CPI setup is oriented to the acquisition of generally demagnified images, as in an ordinary camera. The lack of two synchronized SPAD arrays has imposed using two halves of a single SPAD array as the two sensors D_a and D_b . This entails some constraints to the setup design: demagnified images can only be obtained if the two CPI paths are separated upstream of the lens, rather than downstream (as reported in Fig. 1, and originally proposed in Ref. [46]). The experimental setup thus consists of two main parts (Fig. 3):

1. the ultra-fast imaging device, made of a camera lens (Navitar MVL75M1, of focal length 75 mm and focal ratio 2.8) mounted on the SPAD array sensor;
2. a “CPI adapter”, represented in Fig. 3 by the dashed gray rectangle.

The CPI adapter endeavors the ultra-fast camera with plenoptic properties by first creating (through the first polarizing beam-splitter) and then recombining (through the second polarizing beam-splitter) two optical paths, which we shall indicate as a (depicted in green) and b (depicted in red). Each optical path contains a delay line, offering the required flexibility for choosing the two arbitrary planes O_a and O_b , when preparing the acquisition. In our setup the distances between the planes $O_{a,b}$ and the lens are $z_a = 345$ mm and $z_b = 293$ mm, respectively. The delay lines are made by the combined system ($QM_{a,b}$) of a quarter-wave plate (QWP) and a

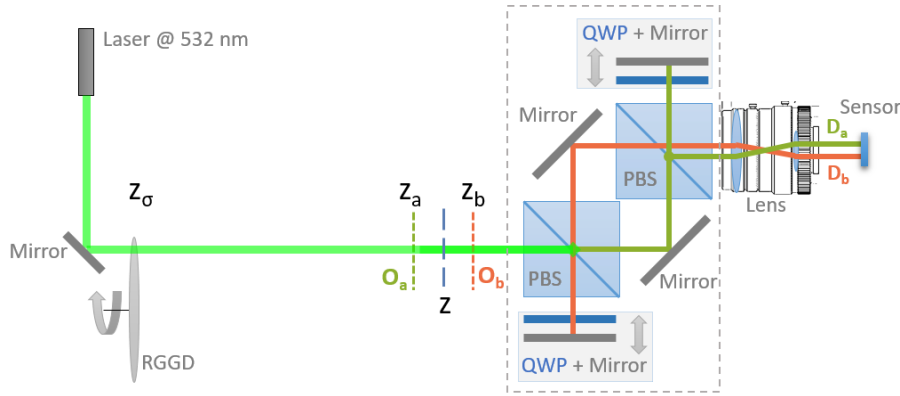


Fig. 3. Technical scheme of the developed CPI setup. The chaotic source is made of a diode laser illuminating a rotating ground glass disk. Two planes, O_a and O_b , arbitrarily chosen in the surrounding of the scene of interest, are imaged by a unique lens onto two disjoint high-resolution detectors D_a and D_b , which are practically implemented by using two halves of the same SwissSPAD2 sensor. Two optical paths, one for each detector, are realized by means of two polarizing beams splitters (PBS), two quarter-wave plates (QWP) and four mirrors; each pair of QWP and mirror is mounted on a translation stage, which offers flexibility in the choice of the two planes O_a and O_b , when preparing the acquisition.

mirror. This combined system converts light from H-polarized to V-polarized, and viceversa, so that the beam that is back-reflected by $QM_{a,b}$ is then reflected/transmitted by the corresponding PBS toward the camera lens. Changing the optical path in arms a and b defines the specific plane to be imaged on sensor D_a and D_b , respectively. In fact, given the lens focal length f and the fixed lens-to-sensor distance z_i , the distance z_o of the object plane from the lens is uniquely defined by the thin lens equation. Hence, the two planes O_a and O_b , imaged on D_a and D_b , respectively, are both placed at an optical distance z_o from the lens; however, the actual planes that are imaged on two disjoint halves of the sensor, are determined by length of the delay lines, which enable to arbitrarily choose the distances z_a and z_b , associated with two different planes within the volume of interest. We should specify that the versatility in choosing the two planes is a useful feature when setting up the acquisition, since it allows the experimenter both to select the planes to be focused and to define the volume that can be refocused (as defined by the blue curve in Fig. 2(b)); the specific choice, however, plays no role during the acquisition itself. Both delay lines are characterized by the same magnifications $M = -z_i/z_o$, numerical aperture (NA), and resolution at focus, as defined by the camera lens. The clear aperture of both the polarizing beam splitter, PBS (45 mm), and the optics (2 inches) in the delay lines have been chosen to enable fully exploiting the NA of the camera lens. In order to maximize its fill factor, the SwissSPAD2 sensor is equipped with a microlens array; its $NA \approx 0.25$ is larger than the lens NA on the image side ($NA_i = NA_o/|M| = 0.13$) and does not limit the NA of the CPI device. However, the pixel size of the sensor is larger than the achievable diffraction limited resolution; hence, the setup has a pixel limited resolution of $95 \mu\text{m}$.

In the present experiment, the CPI device was employed to image transmissive planar test targets placed out of focus, as shown in Fig. 2. The targets are illuminated by a chaotic light source of controllable polarization, intensity, and coherence time, made by a green diode laser (Thorlabs CPS532, $\lambda = 532 \text{ nm}$) scattered by a rotating ground glass disk (GGD). At the maximum rotation speed of the GGD (30 Hz), the measured coherence time of the source is $t_{\text{ch}} \approx 15 \mu\text{s}$.

SwissSPAD2 employs a design that provides one of the largest resolutions (512×512

photodiodes operating in Geiger mode) as well as one of the highest sensitivity (50% photon detection probability at 520 nm) and lowest dark count rate (0.26 cps/ μm^2 , equivalent to a median value of less than 10 cps per pixel) combinations among SPADs which are built with standard CMOS-process technologies. Its 10.5% native fill factor is improved by 4-5 times, for collimated light, by means of the use of a microlens array. The output of each frame consists of a binary matrix identifying the pixels that have been triggered by at least one photon. Due to the binary nature of the signal, it is of utmost importance for the reconstruction of intensity correlations to work close to the linear regime [35, 69], in which the probability to detect a photon is proportional to the intensity of the impinging electromagnetic field.

S1. Plenoptic properties of the intensity correlation function

As demonstrated in Ref. [47], plenoptic information is encoded in the correlation function of Eq. (1) in the main text, representing the correlation between the intensity fluctuations reaching two points, of which one is placed on the detector D_a , and the other on the detector D_b . The correlation function reads, up to irrelevant factors that do not depend on either ρ_a or ρ_b ,

$$\Gamma(\rho_a, \rho_b) = \left| \iint A(\rho_o) A^*(\rho'_o) \Psi(\rho_o, \rho'_o, \rho_a, \rho_b) d^2 \rho_o d^2 \rho'_o \right|^2, \quad (\text{S1})$$

where A is the aperture function of the object. The function Ψ can be considered as a “second-order point-spread function”, which determines the correspondence between object points and detector points. By referring to the parameters in Fig. 3 of the main text, and assuming the source emits chaotic light with an average intensity profile $S(\rho_s)$ and negligible transverse coherence, we have

$$\Psi(\rho_o, \rho'_o, \rho_a, \rho_b) = p_a(\rho_o, \rho_a) p_b(\rho'_o, \rho_b) \int S(\rho_s) e^{\frac{ik}{2z_o} [\rho_o^2 - (\rho'_o)^2 - 2(\rho_o - \rho'_o) \cdot \rho_s]} d^2 \rho_s, \quad (\text{S2})$$

with the functions p_j , $j = a, b$, describing field propagation from the object to the detector. Calling P the pupil function of the lens, we obtain

$$p_j(\rho_o, \rho_j) = \int P(\rho_{\ell j}) e^{ikz \phi_j(\rho_o, \rho_{\ell j}, \rho_j)} d^2 \rho_{\ell j} \quad (\text{S3})$$

with

$$\phi_j(\rho_o, \rho_{\ell j}, \rho_j) = \left(\frac{1}{z - z_j + z_o} - \frac{1}{z_o} \right) \frac{\rho_{\ell j}^2}{2} - \left(\frac{\rho_o}{z - z_j + z_o} - \frac{\rho_j}{M z_o} \right) \cdot \rho_{\ell j} \quad (\text{S4})$$

Notice that the differences in phases ϕ_j with respect to the original results described in Ref. [47] are due to the fact that the optical paths are split upstream of the lens, and not downstream.

The plenoptic properties of the correlation function are easily deduced, for example, from the fact that, by applying a stationary-phase approximation to the integrals which defines it, one obtains

$$\Gamma(\rho_a, \rho_b) \sim \left| A \left[\frac{(z_b - z) \rho_a - (z_a - z) \rho_b}{M \Delta z} \right] \right|^4. \quad (\text{S5})$$

Therefore, $\Gamma(\rho_a, \rho_b)$ represents a collection of images of the object, whose shifts and scaling depend on the axial position of the latter. The refocusing process, consisting in properly realigning the images contained in the correlation function, is discussed in the next section.

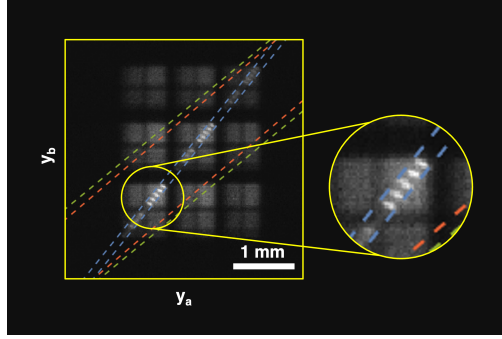


Fig. S1. Two-dimensional correlation function obtained after integration along the x direction of data acquired by the two sensors in the experiment corresponding to case B (as reported in Fig. 2 of the main text). Dashed green and blue lines identify the region (defined by the lens) where non-zero correlations can be found. The dotted blue lines identify the correlated region defined by the light source profile. The overall correlation region is given by the intersection of the three regions.

S2. Refocusing and correlation aperture

In a ray-optics approximation, the correlation function that is measured reads [47, 70, 71]:

$$\begin{aligned} \Gamma(\boldsymbol{\rho}_a, \boldsymbol{\rho}_b) = & \left| A \left[\frac{(z_b - z)\boldsymbol{\rho}_a - (z_a - z)\boldsymbol{\rho}_b}{M\Delta z} \right] \right|^4 \\ & \times \left| P \left[\frac{(z_o + \Delta z)\boldsymbol{\rho}_a - z_o\boldsymbol{\rho}_b}{M\Delta z} \right] \right|^2 \left| P \left[\frac{z_o\boldsymbol{\rho}_a - (z_o - \Delta z)\boldsymbol{\rho}_b}{M\Delta z} \right] \right|^2 \\ & \times \left| S \left[\frac{(z_b - z_o)\boldsymbol{\rho}_a - (z_a - z_o)\boldsymbol{\rho}_b}{M\Delta z} \right] \right|^2 . \end{aligned} \quad (\text{S6})$$

This equation shows that Γ contains information regarding the object aperture A , and that also the lens aperture P and source intensity profile S have effects on the correlation function. Each aperture defines a region inside the correlation space $(\boldsymbol{\rho}_a, \boldsymbol{\rho}_b)$, as shown in Fig. S1: the green and red lines indicate the regions where non-zero correlations can be expected, as defined by the lens; the blue lines, instead, indicate the effects of limited aperture of the source, *i.e.* the width of the Gaussian profile illuminating the GGD. In fact, correlation can only be measured if the light passes through all the apertures, and this means that the correlation region is the intersection of the three correlation regions defined by P and S . By considering only the correlation region, in data analysis, one eliminates all the spurious signal outside that area, which can only be due to noise. Moreover, to simplify the numerical operations, one can consider only the smallest of the regions defined by P and S rather than their intersection (in our case, the area defined by the source). In order to determine the dominating aperture, an effective radius in the correlation space should be evaluated for all the apertures. For the lens of aperture P we consider a circular 2D pupil function with radius equal to the effective radius of the lens: $r_\ell = \text{NA}_o z_o$. If we call *correlation aperture* (CA) the radius of the region defined by the lens, we obtain

$$\text{CA}_{\text{lens},a} = \text{NA}_o \frac{|M\Delta z|}{\sqrt{(1 + \Delta z/z_o)^2 + 1}} \quad \text{CA}_{\text{lens},b} = \text{NA}_o \frac{|M\Delta z|}{\sqrt{(1 - \Delta z/z_o)^2 + 1}} . \quad (\text{S7})$$

The same quantity can be defined and calculated for the source:

$$CA_{\text{source}} = \frac{r_\sigma}{z_\sigma} \frac{|M\Delta z|}{\sqrt{(z_b/z_\sigma - 1)^2 + (z_a/z_\sigma - 1)^2}} \quad , \quad (\text{S8})$$

where $r_\sigma = c \sigma = 1.44$ mm is the radius of the source aperture, that depends on the standard deviation $\sigma = 1.02$ mm of its Gaussian profile. The factor c is used as an optimization parameter to maximize the SNR. To show that the source is the limiting aperture in our experimental conditions, we report the three radii:

$$CA_{\text{lens},a} = 0.63 \text{ mm}, \quad CA_{\text{lens},b} = 0.53 \text{ mm}, \quad CA_{\text{source}} = 0.07 \text{ mm}. \quad (\text{S9})$$

The refocusing $\alpha(z)$ is a linear operator that transforms the coordinates on the detector planes ρ_a and ρ_b into two new ones: ρ_r related to the refocusing plane, and ρ_s related to another generic plane in z_s . It reads:

$$\alpha(z) : \begin{bmatrix} \rho_a \\ \rho_b \end{bmatrix} \mapsto \begin{bmatrix} \rho_r \\ \rho_s \end{bmatrix} = \frac{1}{M\Delta z} \begin{bmatrix} z_b - z & z - z_a \\ z_b - z_s & z_s - z_a \end{bmatrix} \begin{bmatrix} \rho_a \\ \rho_b \end{bmatrix} \quad . \quad (\text{S10})$$

By applying the transformation to the measured correlation function in the position z of the target, one obtains

$$\Gamma_r(\rho_r, \rho_s, z) = \Gamma \left(\alpha^{-1}(z) \begin{bmatrix} \rho_r \\ \rho_s \end{bmatrix} \right) \sim |A(\rho_r)|^4 |S(\rho_s)|^2 \quad . \quad (\text{S11})$$

The last approximate equality stems from the much smaller radius of the source with respect to the lens, so that the latter can be considered irrelevant. We should point out, however, that the algorithm of Eq.(S10) is the most convenient choice only when the source is the limiting aperture and should be modified accordingly if the lens becomes the dominating aperture. The final integration

$$\Sigma(\rho_r, z) = \int \Gamma_r(\rho_r, \rho_s, z) d^2 \rho_s \sim |A(\rho_r)|^4 \quad (\text{S12})$$

can be done by limiting the integration domain to an area defined by the source radius.

By comparing Eqs. (S6) and (S10), we see that the coefficients on which the object aperture depends correspond to the first row of the refocusing matrix, while the second row contains the coefficients that appear in the source profile. The first line gives us an insight into what the refocusing algorithm actually does, that is, rescaling the detector coordinates so that, in the transformed plane, the object depends only on the set of two-dimensional coordinates ρ_r . It is also clear that the second line, defining the variable ρ_s that is integrated in Eq. (S12), plays no relevant role for the object reconstruction, and can be chosen arbitrarily. However, some choices are more convenient than other when defining the integration variable. For example, since the extension of the correlation function is defined by the size of the apertures, a clever choice is to define ρ_s as the transverse coordinate of one of the limiting apertures. By doing so, one can integrate only where non-zero correlations are expected, and limit the integration of Eq. (S12) to a much smaller area than what has been measured, so as to speed up calculations quite dramatically. Given the values of the correlation apertures in Eq. (S9), it made sense to us to choose the integration variable as the one defined by the source. If that were not the case, the second line would have been modified with the coefficients of the aperture defining the major limitation on the correlation area.

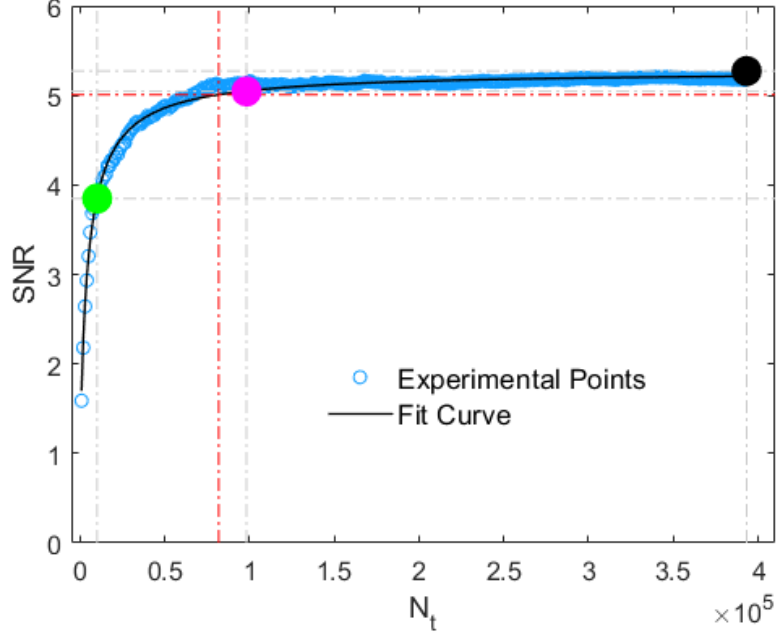


Fig. S2. Behavior of the SNR in the image refocused by CPI (referred to case C shown in Fig. 3 of the main text), as a function of the number of collected frames N_t . Blue circles represent the SNR evaluated on the experimental refocused images, while the solid black line corresponds to the fitting curve $(a + b/N_t)^{-1/2}$. The points discussed in the text, and corresponding to $N_t = 4.0 \times 10^5$, $N_t = 9.8 \times 10^4$, and $N_t = 9.8 \times 10^3$, are highlighted in black, magenta, and green, respectively. The red dotted lines correspond to $N_t = 8 \times 10^4$, where we estimated a decrease of the SNR by 5% of its maximum.

S3. Data analysis workflow

Data analysis has been performed on MATLAB and consisted of two main parts, that are data reading and correlation, and refocusing. In the first part, the binary frames are read from the disk and the correlation function is evaluated by averaging over all frames. Computation of the correlation function is fast and efficient, so that the speed of the process was mostly defined by the data read rate of the disk; reading $\sim 10^4$ frames (512×256) and computing the correlation function took about 200 s. After the correlation function is available in the workstation memory as a 4D array, the operation of refocusing took about 14 s per axial coordinate z .

S4. Study of the SNR dependence on the number of frames

We report in Fig. S2 the full analysis of the dependence of the SNR on the number of frames N_t . The analysis has been performed in the experimental conditions corresponding to case “C” of Fig. 2 (main text). The experimental points indicates that the SNR tends to saturate as the number of frames increases. This behavior deviates from the $\sqrt{N_t}$ scaling, expected if the collected frames were statistically independent, since our source can only provide a finite number of samples. We thus fit the experimental points of the SNR with the function

$$\text{SNR}(N_t) = \frac{1}{\sqrt{a + \frac{b}{N_t}}}, \quad (\text{S13})$$

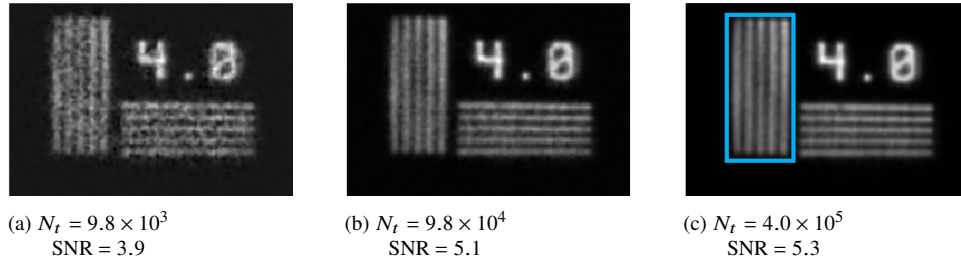


Fig. S3. Comparison of the refocused images acquired at 10 (a) and 1 (b) volumetric images per second. Panel (c) shows the refocused image using the whole acquired dataset. The cyan rectangle indicates the area where the SNR has been evaluated on the three images.

which accounts for both the $\sqrt{N_t}$ behavior at a small number of frames and the saturation at a high number of frames. The best fit provides $a = 3.60 \times 10^{-2}$ and $b = 3.18 \times 10^2$. The plot in Fig. S2 indicates that variations in the number of acquired frames around $N_t = 4.0 \times 10^5$ does not yield an appreciable improvement in image quality. Actually, a reduction of N_t by a factor close to 4 ($N_t = 9.8 \times 10^4$) with respect to the whole dataset, which enables to collect each CPI image in one second ($T_{\text{CPI}} = 1$ s), produces a decrease in the SNR by less than 5%. Moreover, a further reduction in the number of frames to $N_t = 9.8 \times 10^3$, which enables to collect 10 CPI in one second ($T_{\text{CPI}} = 0.1$ s), Fig. S3 shows a comparison between these three cases, with the corresponding estimated values of the SNR. The SNR in the region of interest enclosed in the cyan rectangle highlighted in Fig. S3, has been estimated as

$$\text{SNR} = \frac{\bar{\Sigma}_{\text{in}}}{\Delta_{\text{in}} \Sigma}, \quad (\text{S14})$$

where $\bar{\Sigma}_{\text{in}}$ represents the average value of the signal, in the image, in correspondence of the transmissive parts of the considered five-slit group; the denominator $\Delta_{\text{in}} \Sigma$ represents the standard deviation of the values contributing to the numerator. Such a definition relies on the realistic assumption that the statistical distributions of the signal in the refocused image, in correspondence of the transmissive parts, are identical.

Funding.

Acknowledgments. This research is funded through the project Qu3D, supported by the Italian Istituto Nazionale di Fisica Nucleare (INFN), the Swiss National Science Foundation (grant 20QT21_187716 “Quantum 3D Imaging at high speed and high resolution”), the Greek General Secretariat for Research and Technology, the Czech Ministry of Education, Youth and Sports, under the QuantERA program, which has received funding from the European Union’s Horizon 2020 research and innovation program. G.M., F.V.P., D.G. and M.D. acknowledge partial support by INFN through project PICS4ME. F.S. acknowledges support by Research for Innovation REFIN-Regione Puglia POR PUGLIA FESR-FSE 2014/2020.

Disclosures. FD, FVP and MD: International patent application WO2020/194025 (P), EC: Fastree3D SA (I,S) and PI Imaging Technology SA (I,S), CB: PI Imaging Technology SA (I,S).

Data availability. Data underlying the results presented in this paper are not publicly available at this time but may be obtained from the authors upon reasonable request.

References

1. M. Genovese, “Real applications of quantum imaging,” *J. Opt.* **18**, 073002 (2016).
2. P.-A. Moreau, E. Toninelli, T. Gregory, and M. J. Padgett, “Imaging with quantum states of light,” *Nat. Rev. Phys.* **1**, 367–380 (2019).

3. M. Gilaberte Basset, F. Setzpfandt, F. Steinlechner, E. Beckert, T. Pertsch, and M. Gräfe, “Perspectives for applications of quantum imaging,” *Laser & Photonics Rev.* **13**, 1900097 (2019).
4. G. B. Lemos, V. Borish, G. D. Cole, S. Ramelow, R. Lapkiewicz, and A. Zeilinger, “Quantum imaging with undetected photons,” *Nature* **512**, 409 (2014).
5. R. Meyers, K. S. Deacon, and Y. Shih, “Ghost-imaging experiment by measuring reflected photons,” *Phys. Rev. A* **77**, 041801 (2008).
6. N. D. Hardy and J. H. Shapiro, “Ghost imaging in reflection: resolution, contrast, and signal-to-noise ratio,” *Proc. SPIE* **7815**, 78150L (2010).
7. K. W. C. Chan, M. N. O’Sullivan, and R. W. Boyd, “Two-color ghost imaging,” *Phys. Rev. A* **79**, 033808 (2009).
8. S. Karmakar and Y. Shih, “Two-color ghost imaging with enhanced angular resolving power,” *Phys. Rev. A* **81**, 033845 (2010).
9. D. Kalashnikov, A. Paterova, S. Kulik, and L. A. Krivitsky, “Infrared spectroscopy with visible light,” *Nat. Photon.* **10**, 98–101 (2016).
10. R. E. Meyers, K. S. Deacon, and Y. Shih, “Turbulence-free ghost imaging,” *Appl. Phys. Lett.* **98**, 111115 (2011).
11. D. Shi, C. Fan, P. Zhang, J. Zhang, H. Shen, C. Qiao, and Y. Wang, “Adaptive optical ghost imaging through atmospheric turbulence,” *Opt. Express* **20**, 27992–27998 (2012).
12. M. Bina, D. Magatti, M. Molteni, A. Gatti, L. A. Lugiato, and F. Ferri, “Backscattering differential ghost imaging in turbid media,” *Phys. Rev. Lett.* **110**, 083901 (2013).
13. G. Brida, L. Caspani, A. Gatti, M. Genovese, A. Meda, and I. R. Berchera, “Measurement of sub-shot-noise spatial correlations without background subtraction,” *Phys. Rev. Lett.* **102**, 213602 (2009).
14. G. Brida, M. Genovese, and I. Ruo-Berchera, “Experimental realization of sub-shot-noise quantum imaging,” *Nat. Photonics* **4**, 227–230 (2010).
15. N. Samantaray, I. Ruo-Berchera, A. Meda, and M. Genovese, “Realization of the first sub-shot-noise wide field microscope,” *Light Sci. Appl.* **6**, e17005 (2017).
16. A. Meda, E. Losero, N. Samantaray, F. Scafirimuto, S. Pradyumna, A. Avella, I. Ruo-Berchera, and M. Genovese, “Photon-number correlation for quantum enhanced imaging and sensing,” *J. Opt.* **19**, 094002 (2017).
17. R. W. Boyd and D. Prato, *Nonlinear Optics* (Elsevier Science, Oxford, 2008).
18. T. B. Pittman, Y.-H. Shih, D. V. Strekalov, and A. V. Sergienko, “Optical imaging by means of two-photon quantum entanglement,” *Phys. Rev. A* **52**, R3429 (1995).
19. M. H. Rubin, “Transverse correlation in optical spontaneous parametric down-conversion,” *Phys. Rev. A* **54**, 5349 (1996).
20. R. S. Bennink, S. J. Bentley, and R. W. Boyd, ““Two-photon” coincidence imaging with a classical source,” *Phys. Rev. Lett.* **89**, 113601 (2002).
21. A. Valencia, G. Scarcelli, M. D’Angelo, and Y. Shih, “Two-photon imaging with thermal light,” *Phys. Rev. Lett.* **94**, 063601 (2005).
22. A. Gatti, E. Brambilla, M. Bache, and L. A. Lugiato, “Ghost imaging with thermal light: comparing entanglement and classical correlation,” *Phys. Rev. Lett.* **93**, 093602 (2004).
23. F. Ferri, D. Magatti, A. Gatti, M. Bache, E. Brambilla, and L. A. Lugiato, “High-resolution ghost image and ghost diffraction experiments with thermal light,” *Phys. Rev. Lett.* **94**, 183602 (2005).
24. G. Scarcelli, V. Berardi, and Y. Shih, “Can two-photon correlation of chaotic light be considered as correlation of intensity fluctuations?” *Phys. Rev. Lett.* **96**, 063602 (2006).
25. M. N. O’Sullivan, K. W. C. Chan, and R. W. Boyd, “Comparison of the signal-to-noise characteristics of quantum versus thermal ghost imaging,” *Phys. Rev. A* **82**, 053803 (2010).
26. G. Brida, M. Chekhova, G. Fornaro, M. Genovese, E. Lopaeva, and I. R. Berchera, “Systematic analysis of signal-to-noise ratio in bipartite ghost imaging with classical and quantum light,” *Phys. Rev. A* **83**, 063807 (2011).
27. R. S. Aspden, D. S. Tasca, R. W. Boyd, and M. J. Padgett, “EPR-based ghost imaging using a single-photon-sensitive camera,” *New J. Phys.* **15**, 073032 (2013).
28. F. V. Pepe, F. Di Lena, A. Mazzilli, E. Edrei, A. Garuccio, G. Scarcelli, and M. D’Angelo, “Diffraction-limited plenoptic imaging with correlated light,” *Phys. Rev. Lett.* **119**, 243602 (2017).
29. G. Massaro, D. Giannella, A. Scagliola, F. Di Lena, G. Scarcelli, A. Garuccio, F. V. Pepe, and M. D’Angelo, “Light-field microscopy with correlated beams for extended volumetric imaging at the diffraction limit,” *Sci. Rep.* **12**, 16823 (2022).
30. B. I. Erkmen and J. H. Shapiro, “Signal-to-noise ratio of Gaussian-state ghost imaging,” *Phys. Rev. A* **79**, 023833 (2009).
31. E. Lantz, P.-A. Moreau, and F. Devaux, “Optimizing the signal-to-noise ratio in the measurement of photon pairs with detector arrays,” *Phys. Rev. A* **90**, 063811 (2014).
32. G. Scala, M. D’Angelo, A. Garuccio, S. Pascasio, and F. V. Pepe, “Signal-to-noise properties of correlation plenoptic imaging with chaotic light,” *Phys. Rev. A* **99**, 053808 (2019).
33. G. Massaro, G. Scala, M. D’Angelo, and F. V. Pepe, “Comparative analysis of signal-to-noise ratio in correlation plenoptic imaging architectures,” arXiv preprint, arXiv:2206.13412 (2022).
34. L. Mandel and E. Wolf, *Optical coherence and quantum optics* (Cambridge University Press, Cambridge, 1995).
35. I. M. Antolovic, S. Burri, R. A. Hoebe, Y. Maruyama, C. Bruschini, and E. Charbon, “Photon-counting arrays for time-resolved imaging,” *Sensors* **16**, 1005 (2016).

36. A. C. Ulku, C. Bruschini, I. M. Antolovic, Y. Kuo, R. Ankri, S. Weiss, X. Michalet, and E. Charbon, "A 512×512 SPAD Image Sensor with Integrated Gating for Widefield FLIM," *IEEE J. Sel. Top. Quantum Electron* **25**, 6801212 (2019).
37. A. C. Ulku, A. Ardelean, I. M. Antolovic, S. Weiss, E. Charbon, C. Bruschini, and X. Michalet, "Wide-field time-gated SPAD imager for phasor-based FLIM applications," *Methods Appl. Fluoresc.* **98**, 024002 (2020).
38. F. Madonini, F. Severini, F. Zappa, and F. Villa, "Single photon avalanche diode arrays for quantum imaging and microscopy," *Adv. Quantum Technol.* **4**, 2100005 (2021).
39. G. Lubin, R. Tenne, I. M. Antolovic, E. Charbon, C. Bruschini, and D. Oron, "Quantum correlation measurement with single photon avalanche diode arrays," *Opt. Express* **27**, 32863–32882 (2019).
40. H. Defienne, J. Zhao, E. Charbon, and D. Faccio, "Full-field quantum imaging with a single-photon avalanche diode camera," *Phys. Rev. A* **103**, 042608 (2021).
41. V. Salari, D. Paneru, E. Saglamyurek, M. Ghadimi, M. Abdar, M. Rezaee, M. Aslani, S. Barzanjeh, and E. Karimi, "Quantum Face Recognition Protocol with Ghost Imaging," arXiv preprint, arXiv:2110.10088 (2021).
42. X. Gao, Y. Zhang, A. D'Errico, K. Heshami, and E. Karimi, "High-speed imaging of spatiotemporal correlations in Hong-Ou-Mandel interference," *Opt. Express* **30**, 19456–19464 (2022).
43. C. Abbattista, L. Amoruso, S. Burri, E. Charbon, F. Di Lena, A. Garuccio, D. Giannella, Z. Hradil, M. Iacobellis, G. Massaro *et al.*, "Towards quantum 3d imaging devices," *Appl. Sci.* **11**, 6414 (2021).
44. M. D'Angelo, F. V. Pepe, A. Garuccio, and G. Scarcelli, "Correlation plenoptic imaging," *Phys. Rev. Lett.* **116**, 223602 (2016).
45. F. V. Pepe, F. Di Lena, A. Garuccio, G. Scarcelli, and M. D'Angelo, "Correlation plenoptic imaging with entangled photons," *Technologies* **4**, 17 (2016).
46. F. Di Lena, F. V. Pepe, A. Garuccio, and M. D'Angelo, "Correlation Plenoptic Imaging: An Overview," *Appl. Sci.* **8**, 1958 (2018).
47. F. Di Lena, G. Massaro, A. Lupo, A. Garuccio, F. V. Pepe, and M. D'Angelo, "Correlation plenoptic imaging between arbitrary planes," *Opt. Express* **28**, 35857–35868 (2020).
48. A. Scagiola, F. Di Lena, A. Garuccio, M. D'Angelo, and F. V. Pepe, "Correlation plenoptic imaging for microscopy applications," *Phys. Lett. A* p. 126472 (2020).
49. R. Ng, M. Levoy, M. Brédif, G. Duval, M. Horowitz, and P. Hanrahan, "Light field photography with a hand-held plenoptic camera," *Comput. Sci. Tech. Rep. CSTR* **2**, 1–11 (2005).
50. R. Ng, *Digital light field photography* (Stanford University, California, 2006).
51. T. Georgiev and C. Intwala, "Light field camera design for integral view photography," Adobe Syst. Inc., Tech. Rep. (2006).
52. T. G. Georgiev and A. Lumsdaine, "Focused plenoptic camera and rendering," *J. Electron. Imaging* **19**, 021106 (2010).
53. T. Georgeiv, K. C. Zheng, B. Curless, D. Salesin, S. Nayar, and C. Intwala, "Spatio-angular resolution tradeoffs in integral photography," in *Proceedings of the 17th Eurographics Conference on Rendering Techniques*, (Eurographics Association, Goslar, DEU, 2006), EGSR '06, p. 263–272.
54. D. G. Dansereau, O. Pizarro, and S. B. Williams, "Decoding, calibration and rectification for lenselet-based plenoptic cameras," in *Proceedings of the IEEE conference on computer vision and pattern recognition*, (2013), pp. 1027–1034.
55. J. Pérez, E. Magdaleno, F. Pérez, M. Rodríguez, D. Hernández, and J. Corrales, "Super-resolution in plenoptic cameras using FPGAs," *Sensors* **14**, 8669–8685 (2014).
56. Y. Li, M. Sjöström, R. Olsson, and U. Jennehag, "Scalable coding of plenoptic images by using a sparse set and disparities," *IEEE Trans. on Image Process.* **25**, 80–91 (2016).
57. R. Ng, "Fourier slice photography," *ACM Trans. on Graph.* **24**, 735–744 (2005).
58. M. Broxton, L. Grosenick, S. Yang, N. Cohen, A. Andalman, K. Deisseroth, and M. Levoy, "Wave optics theory and 3-D deconvolution for the light field microscope," *Opt. Express* **21**, 25418–25439 (2013).
59. R. Prevedel, Y.-G. Yoon, M. Hoffmann, N. Pak, G. Wetzstein, S. Kato, T. Schrödel, R. Raskar, M. Zimmer, E. S. Boyden *et al.*, "Simultaneous whole-animal 3d imaging of neuronal activity using light-field microscopy," *Nat. Methods* **11**, 727–730 (2014).
60. O. Skocek, T. Noebauer, L. Weiglun, F. Martínez Traub, C. Xia, M. Molodtsov, A. Grama, M. Yamagata, D. Aharoni, D. Cox, P. Golshani, and A. Vaziri, "High-speed volumetric imaging of neuronal activity in freely moving rodents," *Nat. Methods* **15**, 429–432 (2018).
61. T. Zhu, L. Zhu, Y. Li, X. Chen, M. He, G. Li, H. Zhang, S. Gao, and P. Fei, "High-speed large-scale 4D activities mapping of moving *C. elegans* by deep-learning-enabled light-field microscopy on a chip," *Sens. Actuators B Chem.* **348**, 130638 (2021).
62. F. Scattarella, M. D'Angelo, and F. V. Pepe, "Resolution limit of correlation plenoptic imaging between arbitrary planes," *Optics* **3**, 138–149 (2022).
63. G. Massaro, F. V. Pepe, and M. D'Angelo, "Refocusing Algorithm for Correlation Plenoptic Imaging," *Sensors* **22**, 6665 (2022).
64. O. Katz, Y. Bromberg, and Y. Silberberg, "Compressive ghost imaging," *Appl. Phys. Lett.* **95**, 131110 (2009).
65. L. Jiying, Z. Jubo, L. Chuan, and H. Shisheng, "High-quality quantum-imaging algorithm and experiment based on compressive sensing," *Opt. letters* **35**, 1206–1208 (2010).
66. J. Reháček, Z. Hradil, M. Zawisky, W. Treimer, and M. Strobl, "Maximum-likelihood absorption tomography," *EPL*

- 59**, 694 (2002).
67. Z.-M. Li, S.-B. Wu, J. Gao, H. Zhou, Z.-Q. Yan, R.-J. Ren, S.-Y. Yin, and X.-M. Jin, "Fast correlated-photon imaging enhanced by deep learning," *Optica* **8**, 323–328 (2021).
 68. F. Ferri, D. Magatti, L. Lugiato, and A. Gatti, "Differential ghost imaging," *Phys. Rev. Lett.* **104**, 253603 (2010).
 69. I. M. Antolovic, C. Bruschini, and E. Charbon, "Dynamic range extension for photon counting arrays," *Opt. Express* **26**, 22234–22248 (2018).
 70. F. V. Pepe, G. Scarcelli, A. Garuccio, and M. D'Angelo, "Plenoptic imaging with second-order correlations of light," *Quantum Meas. Quantum Metrol.* **3**, 20–26 (2016).
 71. G. Massaro, F. Di Lena, M. D'Angelo, and F. V. Pepe, "Effect of finite-sized optical components and pixels on light-field imaging through correlated light," *Sensors* **22** (2022).